SPATIAL DISTRIBUTION OF SHALLOW CRUSTAL ANISOTROPY FROM SHEAR WAVE SPLITTING MEASUREMENTS AT THE ENDEAVOUR SEGMENT OF THE JUAN DE FUCA RIDGE

by

KOHTARO ARARAGI

A THESIS

Presented to the Department of Geological Sciences
and the Graduate School of the University of Oregon
in partial fulfillment of the requirements
for the degree of
Master of Science

March 2012

THESIS APPROVAL PAGE

Student: Kohtaro Araragi

Title: Spatial Distribution of Shallow Crustal Anisotropy from Shear Wave Splitting Measurements at the Endeavour Segment of the Juan de Fuca Ridge

This thesis has been accepted and approved in partial fulfillment of the requirements for the Master of Science degree in the Department of Geological Sciences by

Eugene D. Humphreys	Chairperson
Douglas R. Toomey	Member
Emilie E. E. Hooft	Member

and

Kimberly Andrews Espy	Vice President for Research & Innovation/Dean of the Graduate School

Original approval signatures are on file with the University of Oregon Graduate School.

Degree awarded March 2012

THESIS ABSTRACT

Kohtaro Araragi

Master of Science

Department of Geological Sciences

March 2012

Title: Spatial Distribution of Shallow Crustal Anisotropy from Shear Wave Splitting Measurements at the Endeavour Segment of the Juan de Fuca Ridge

We investigate upper crustal anisotropy of the Endeavour Segment of the Juan de Fuca Ridge using shear wave splitting measurements of ~3000 earthquakes recorded during three years using the Keck seafloor seismic network. We apply a new cluster analysis of shear-wave splitting measurements to our database. The methodology reduces the use of subjective criteria and improves the accuracy of measurements in the presence of noisy data. Fast polarization directions at a given seismic station are constant and stable during the deployment; however, fast-polarization directions between stations vary significantly. We presume that the lack of consistency of shear wave splitting among seismic stations reflects the spatial distribution of anisotropy in the vicinity of the ridge axis. We infer that the variation of fast polarization directions and delay times is caused by spatial variations in shallow hydrogeological structures and the stress field. Local faults and fissures are unlikely to be the primary cause of this anisotropy since most of the fast polarization directions are not consistent with the ridge parallel trend of faults. Stress perturbations induced by magmatic injection into the axial magma chamber or spatial variation in the rates of a hydrothermal heat transfer may contribute to the observed heterogeneity in seismic anisotropy.

CURRICULUM VITAE

NAME OF AUTHOR: Kohtaro Araragi

GRADUATE AND UNDERGRADUATE SCHOOOLS ATTENDED:

University of Oregon, Eugene, OR, USA

Kyushu University, Fukuoka, Japan

DEGREES AWARDED:

Master of Science, Geological Sciences, 2012, University of Oregon

Master of Engineering, Engineering, 2009, Kyushu University

AREA OF SPECIAL INTEREST:

Hydrothermal systems

Evolution of hydrothermal systems accompanied by magmatic intrusions.

Seismology

Seismic anisotropy in the upper oceanic crust.

ACKNOWLEDGEMENTS

I would like to express my best gratitude to Douglas Toomey who gave me with this fantastic project that relating to seismology and hydrothermal systems. I could spend the most exciting time in my life thanks our nice collaboration. I would like to thank Emilie Hooft. Her open attitude for the discussion helped me a lot when I had some problems. I acknowledge William Wilcock and Robert Weekly. My basic understanding of the Keck Seismic experiment owes to their effort. Martha Savage kindly provided me with a new shear wave splitting code. I thank the critical discussions with her through my research. Eugene Humphreys helped me a lot for consideration of shear wave splitting from viewpoints of the most important principles of geophysics. He also worked as the chair of thesis committee. I strongly believe that my sense of geophysics improved a lot by discussions with him. In addition to my thesis committee, I appreciate help of Ray Weldon and Mark Reed. Their advice improved the quality of my job as a graduate student of the Department of Geological Sciences. Also, I appreciate big help from instructors of the American English Institution, Robert Elliot and Keli Yelian. They helped me to improve my English a lot and I could not imagine my graduate study without them. I thank J. Delaney and D. Kelley for their leadership of the program that included this experiment. The W. M. Keck Foundation supported the seismic and hydrothermal data collection and analysis with matching support from the Monterey Bay Aquarium (for ship time and ocean bottom instruments) and the University of Washington (UW) (for ship time). The National Science Foundation (NSF) supported this research (OCE‐0937285) as well as the computational facility at the University of Oregon (EAR‐0651123)

TABLE OF CONTENTS

LIST OF FIGURES

LIST OF TABLES

CHAPTER I

INTRODUCTION

Tectonic extension, magmatic intrusion, and hydrothermal circulation affect the stress field near mid-ocean ridges. Our understanding of these processes can be improved if we can constrain crustal stress. The Endeavour Segment of the Juan de Fuca Ridge (Figure 1) is an intermediate spreading ridge where faulting occurs along the ridge axis and an axial magma chamber maintains hydrothermal circulations along the faults and fissures (Carbotte et al., 2006; Van Ark et al., 2007). Several geologic processes, which are likely to influence crustal stress, have been reported in the area. Magmatic injections into a sill at the ridge axis can cause stress perturbations and increase the rate of local seismicity (Wilcock et al., 2009) while diking events may result in faulting and formation of a graben along the ridge axis (Carbotte et al., 2006). In February 2005, a large earthquake swarm along the northern portion of the Endeavour Segment was also thought to have occurred by magmatic activity (Hooft et al., 2010). All of these events contribute to crustal stresses at the Endeavour Segment.

Observations of crustal seismic anisotropy can provide constraints on the stress field. For example, fractures in the crust often form parallel to the orientation of minimum compressive stress. Seismic anisotropy can be measured with shear wave splitting, which separates observed S phases into distinct components polarized in the fast (ϕ) and slow anisotropy orientations and measures the delay time (δt). Shear wave splitting observations thus provide information about stress-aligned crack orientations. Temporal changes in seismic anisotropy have also been used to detect changes in stress caused by upper crustal events (e.g. Gerst and Savage, 2004; Johnson et al, 2010; Roman et al., 2011). Stress perturbations induced by magmatic or tectonic events at the

Endeavour Segment may thus be investigated by measuring anisotropy before and after major geologic events.

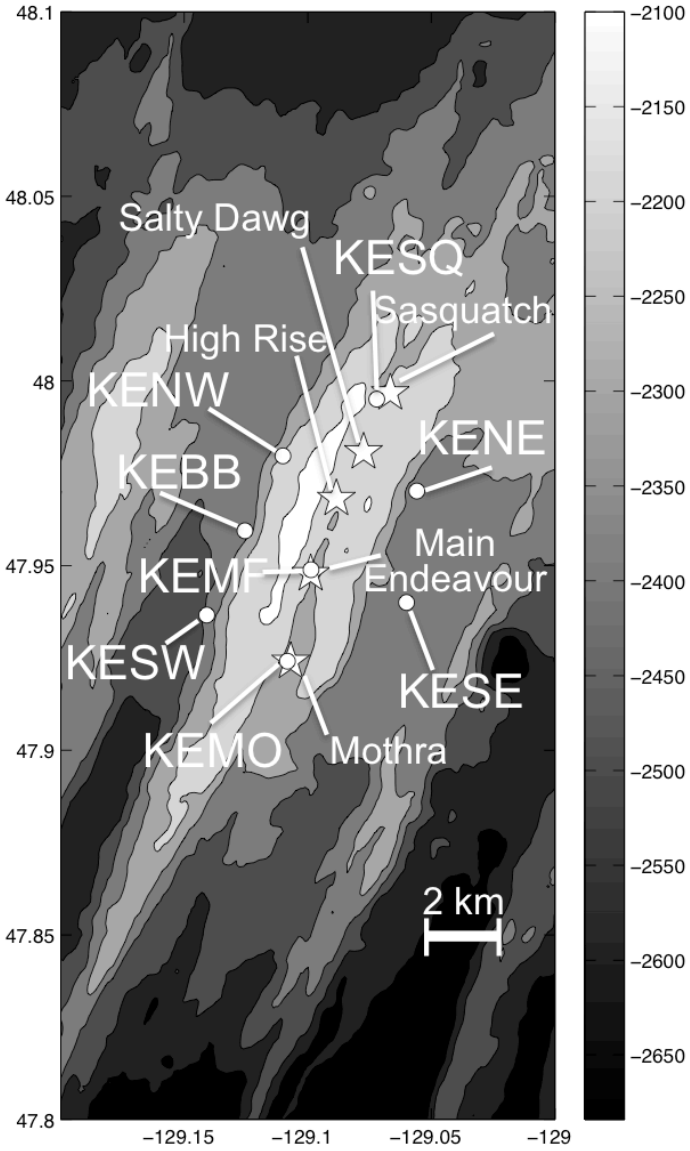

Figure 1. Map of Endeavour segment showing the Keck OBS network. Circles indicate seismometers and stars show the locations of hydrothermal vent fields.

Here we present shear wave splitting measurements of the Keck seismic database from August 2003 to August 2006. Measuring shear wave splitting can be a time consuming process and it is difficult to maintain objective and constant criteria for a large database. For example, the application of multiple filters is necessary not only for verification but also for overcoming the frequency dependence of shear wave splitting (e.g. Marson-Pidgeon and Savage, 1997; Gerst and Savage, 2004; Liu et al, 2006). To reduce the subjectivity inherent to shear wave splitting measurements, we use a new automated measurement technique (Savage et al., 2010) to investigate seismic anisotropy of the Endeavour segment to constrain the local stress field. We apply this method to the Keck seismic database, which includes ~40,000 earthquakes recorded along the Endeavour Segment. Our results show that the fast polarization directions observed across the seismic array are not consistently parallel to the ridge axis. For our data set, most of the earthquakes occur beneath the Main Endeavour vent field, thus the seismic waves sample the crust at a site of intense hydrothermal activity. Since at the regional scale it is likely that the stress field is dominantly extensional, the inter-station variability in the observed fast polarization directions suggests that the center of the Endeavour Segment is influenced by processes that perturb the local stress field.

CHAPTER II

BACKGROUND OF THE ENDEAVOUR SEGMENT AND SEISMIC DATA

Section 2.1. Geological Setting of the Endeavour Segment

The Juan de Fuca Ridge is an intermediate-rate spreading center (~ 5.7cm/yr, DeMets et al., 1994). There are five high temperature vent fields in the central portion of the Endeavour Segment and extensive seismicity is observed in the area (e.g. Wilcock et al., 2002; Wilcock et al., 2009). The seismicity above the magma chamber (Figure 2) results from a combination of tectonic extensional stresses, magmatic processes and hydrothermal circulation (McClain et al., 1993; Wilcock and Delaney, 1996; Wilcock et al., 2002; Wilcock et al., 2009). Hydrothermal circulation extracts a significant amount of heat from the magmatic system (e.g. Wilcock and Delaney, 1996). Repeated dike events from the axial magma chamber, in combination with plate spreading, cause faulting along the ridge axis (e.g. Van Ark et al., 2007). The stability of hydrothermal circulation is inferred from the scale and location of hydrothermal vents along the ridge axis (e.g. Delaney et al. 1992; Wilcock and Delaney, 1996; Van Ark et al., 2007). In addition to the influence of dike intrusion on the hydrothermal system, the rheological interaction of diking and faulting is inferred to play a dominant role in the formation of oceanic crust (Carbotte et al., 2006).

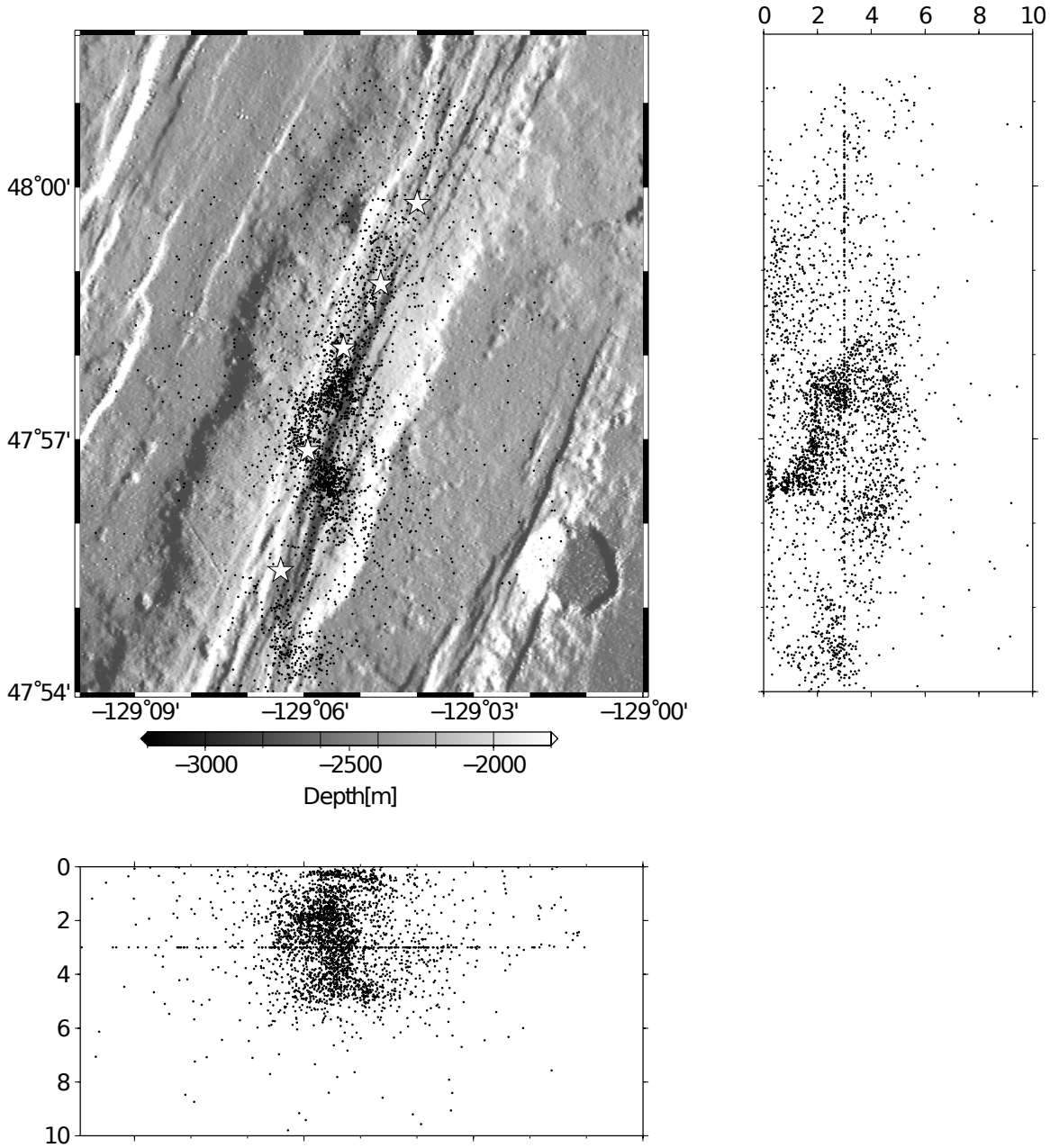

Figure 2. Bathymetric map showing earthquakes used for measurements. Black dots indicate epicenters. We restrict our analysis to events within 3 km of the closest OBS. Stars indicate the location of known hydrothermal vent fields.

Section 2.2. Keck Seismic Experiment

The Keck seismic network was deployed along the central portion of the Endeavour Segment of the Juan de Fuca Ridge from August 2003 to October 2006 (Figure 1). The seismic network comprised seven short-period seismometers (Mark Products L-28B geophones) and one broadband seismometer (Guralp CMG-1T). Five instruments were placed in core holes drilled into pillow basalts (Stakes et al., 1998) while three instruments, including the broadband sensor, were installed at sedimented sites. During the deployment of the seismic network, an earthquake swarm occurred in February 2005 (Hooft et al., 2010). The total number of earthquakes observed during the experiment is over 38,000. We choose approximately 3000 well-located events, which are located close to the Keck seismic network, for our analysis of shear wave splitting.

CHAPTER III

METHODOLOGY

We use an automated method to measure shear wave splitting. The advantages of an automated method are that it provides a means to maintain objective and consistent criteria for measuring shear wave splitting and it allows the analysis of large volumes of data. We use the method of Savage et al. (2010), which uses multiple windows and frequency bands to measure splitting and evaluates the results using a clustering algorithm (Savage et al., 2010; Teanby et al., 2004). The technique applies 14 different filters and determines the best three filters that have the highest value of the product of the signal-to-noise ratio (SNR) and the filter bandwidth. The method applies the best three filters to the seismic data and measures shear wave splitting using the approach of Silver and Chan (1991). The clustering algorithm calculates shear wave splitting by shifting a measurement window of variable length along the seismic traces within a defined range and then determines the best result from the tightest cluster of measurements. The distribution of clusters is evaluated and the results from scattered clusters are rejected.

The automated method requires the user to choose several parameters; examples are discussed by Savage et al. (2010). The lengths of trial measurement windows are determined on the basis of the dominant frequency, as measured from the maximum amplitude of the fast Fourier transform of the seismic data. This allows the length of windows to be adjusted for each event. In addition, particularly noisy data should be rejected beforehand. The size of measurement windows of the SNR are assigned shorter than the S-P time at each station and other parameters for the measurement window (Table 1) are determined based on the dominant frequency of each seismic station so that the measurement windows do not include phases arriving after the S-phase.

	tlagmax	fdmin	Fdmax	filter model	SNRwindow	SNRmax	t_win_freq	offset
KESQ	0.3	3	6	A	0.3	5	0.45	0.2
KEMO	0.3	3	10	A	0.3	3	0.45	0.2
KEMF	0.3	3	10	B	0.3	5	0.45	0.2
KENW	0.3	4	8	B	0.3	5	0.45	0.2
KENE	0.3	4	10	A	0.3	5	0.45	0.2
KESE	0.3	3	10	B	0.3	3	0.45	0.2
KESW	0.3	4	10	B	0.3	3	0.45	0.2
KEBB	0.4	1.5	5	B	0.3	3	0.45	0.35

Table 1. Parameters for shear wave splitting measurements. We chose parameters for measurements based on the features of the waveforms. Anisotropy in the upper crust is assumed to be small (<0.3 s) (Savage, 1999). We determined maximum delay time (tlagmax) as less than 0.3 or 0.4 (tlagmax). SNR window ("SNR window" in Figure 3) and a small offset before S-time (see "offset" in Figure 3) is determined from estimated S-wave train and S-P time. We calculated the estimated range of measurement windows and determined maximum and minimum threshold value of dominant frequency.

SNR is used as an indicator of S-phases that are affected by P-coda or environmental noise. We define the size of noise windows from P times to S times (noise window, Figure 3). We determine the size of signal windows (SNR window, Figure 3) to be 0.3 s so that it does not exceed the S-P times and dominant S-phase.

The lengths of measurement windows are determined so that they include just a few cycles of the S-phase. The time of the end of measurement windows are defined as S-time + 1/(dominant frequency) *constant. The constant of our measurements are 1/1.2 in the start windows (Figure 4a, line 3) and 2.0 in the end windows (Figure 4a, line 4). We determine the maximum and minimum frequency (fdmin and fdmax in Table 1) so that they include the dominant frequencies.

We prepare two sets of filters (Table 2). Model A is used for stations KESQ, KEMO, and KENE while model B is used for stations KEMF, KENW, KESE, KEBB and KESW. We prepared the model B filters to be slightly lower than the model A filters because higher frequencies (>15Hz) seemed to be more affected by noise on some stations.

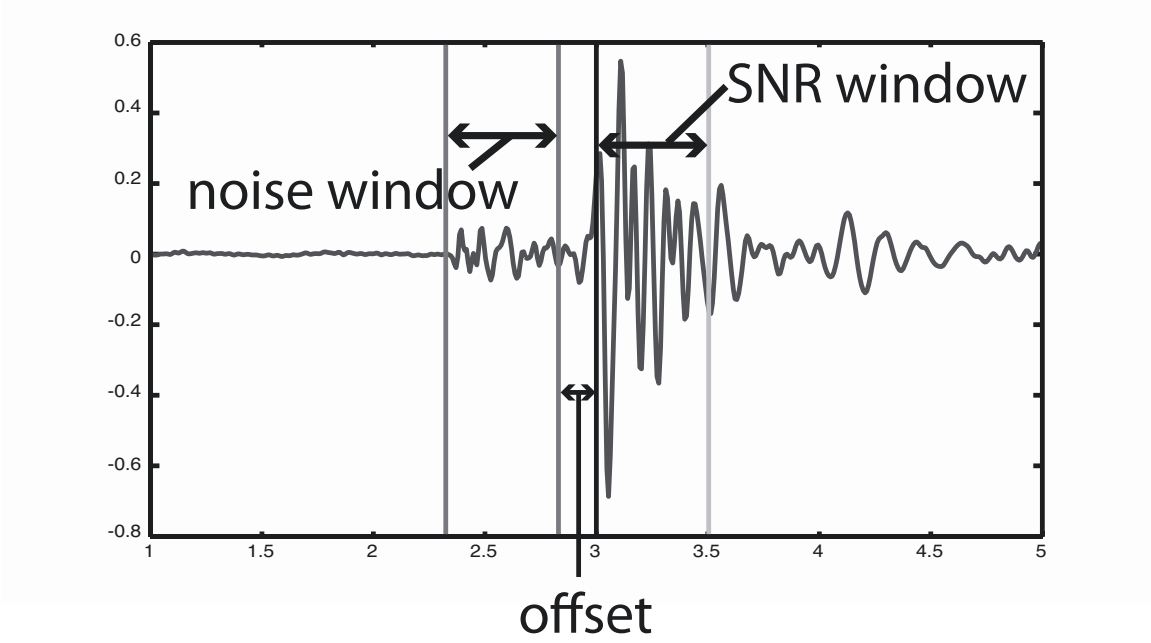

Figure 3. Measurement windows for signal-to-noise ratio (SNR). SNR is calculated as the ratio of the average of absolute value of signals (after S time) to noise (before S time) whose durations are shown as "SNR window", and "noise window", respectively. S-time is shown as the solid black line. We do not use the range of "offset" to avoid the slightly early S arrival. The offset before S-time is determined by trial and error within the range in which the start of the SNR window does not exceed P-time.

In order to obtain good measurements, we make the following manual checks on a subset of data to verify the processing (e.g. corrected waveforms, and error surface):

1) We check that the length of the measurement windows do not include phases arriving after the primary S wave (Figure 4a, line 4).

2) We examine the effect of different filters to ensure that noise is adequately suppressed.

3) We verify that the automated procedure results in corrected particle motions that are liner (e.g. Figure 4b, bottom right).

4) Distribution of error surfaces. Good measurements result in higher contour values (e.g. Figure 4c). Small contour values are often observed at bad measurements. (e.g. Figure 4d)

5) We check that manual and automated processing gives similar results. If the results are not consistent, we adjust the parameters for the automated processing accordingly.

Using the criteria above we determine an acceptable set of parameters (Table 1). Lastly, we determine the best parameters by checking the number of measurements that have consistent measurements from the three best filters and by manual checks of measured results.

We restrict our analysis to events that have depth less than 6.0 km were located using at least 7 P and/or S arrivals and that occurred within 10 km of the OBS station recording the events. The criteria for the number of observed phases generally ensure that the event was large enough to provide good quality waveforms. These criteria greatly reduce a number of smaller events that are generally associated with low signal-to-noise data.

In some cases data are rejected because they do not have measurable shear wave splitting. Following Savage et al. (2010), we compare calculation results from each event. If the results from one arrival have similar values at each filter setting and good cluster grades, the measurement is accepted. In this case we choose the result that has the smallest error bars of ϕ and δt. We reject results when the ratio of the maximum to minimum value of the error surface is less than 8, following Savage et al. (2010).

Model A	lo [Hz]	hi [Hz]	Model B	lo [Hz]	hi [Hz]
1	4	24	1	1	4
2	2	10	2	1	7
3	1	7	3	1	12
4	2	8	4	2	8
5	2	16	5	2	10
6	3	12	6	2	16
7	3	20	7	3	8
8	4	16	8	3	12
9	4	20	9	3	16
10	5	20	10	4	12
11	3	18	11	4	16
12	5	15	12	5	12
13	5	25	13	5	16
14	3.5	21	14	5	20

Table 2. Filters applied to waveforms prior to SWS analysis. We prepared two sets of filters. The filters are designed to include a wider range of frequencies (model A). However, if the data are noisy, we reduce the higher frequency contents (model B).

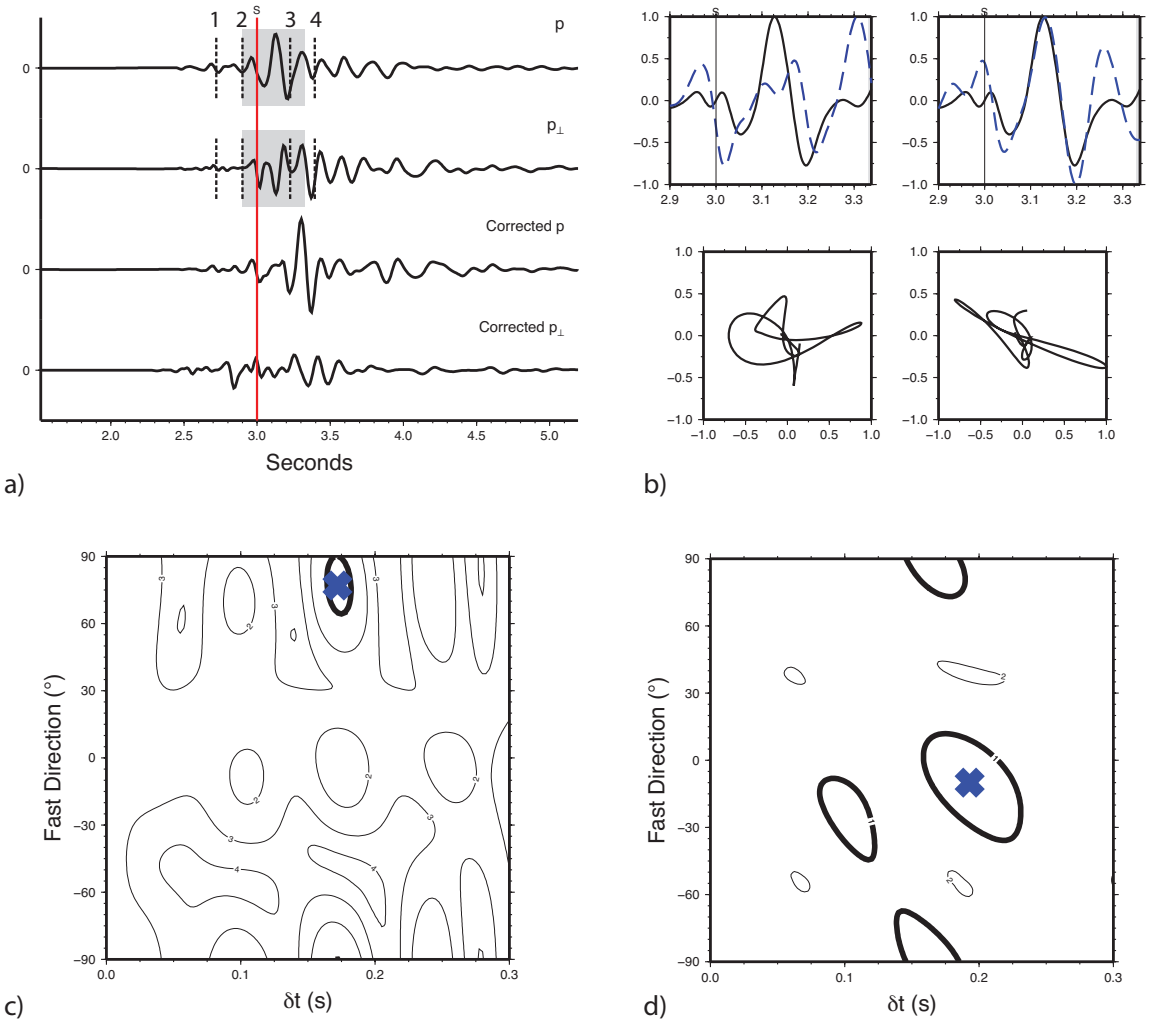

Figure 4. Illustration of shear wave splitting measurements on seismic data. a) The radial and transverse waveforms before and after corrections for Δt and ø. The waveforms are rotated onto the source polarization direction. Dashed lines are the range of measurement windows (see text). b) The original waveforms rotated into ø (left) and corrected waveforms by Δt (right). The rotated wave forms (top) and particle motions (bottom). If the splitting correction succeeds, the particle motion becomes linear. c) Error surface with higher value. d) Error surface with lower value.

CHAPTER IV

MEASUREMENT RESULTS

We measured shear wave splitting for data recorded from August 2003 to August 2006. We could obtain data in the first year at all stations. Data at stations KENW, KENE, KESE and KESW are available after the first year. Limited amount of data have measureable SWS at station KESQ and KEMO in the last year. We begin by showing the results for the first year of recording, which is prior to several significant earthquake swarms, and then we evaluate evidence for any temporal changes in the fast polarization directions throughout the entire deployment period.

Figure 5 shows the fast polarization directions from data between August 2003 and August 2004. For many of the Keck stations, the fast polarization directions do not align parallel to the ridge axis. The rose diagram for all stations (Figure 5, upper right) indicates collectively the fast polarization direction is oriented either at N30˚W or N90˚E. A rose diagram for all stations, however, is dominated by results from station KEMF and KESW. The fast polarization directions for stations KESQ, KEMF, and KEBB trend northwest; however, the trends of fast polarization directions at stations KESE, KEMO and KESW are notably different. The trend at station KESE aligns in the north-south direction while trends at stations KESW and KEMO are directed to the east. Only stations KENE and KENW show a fast polarization direction that aligns approximately parallel to the ridge.

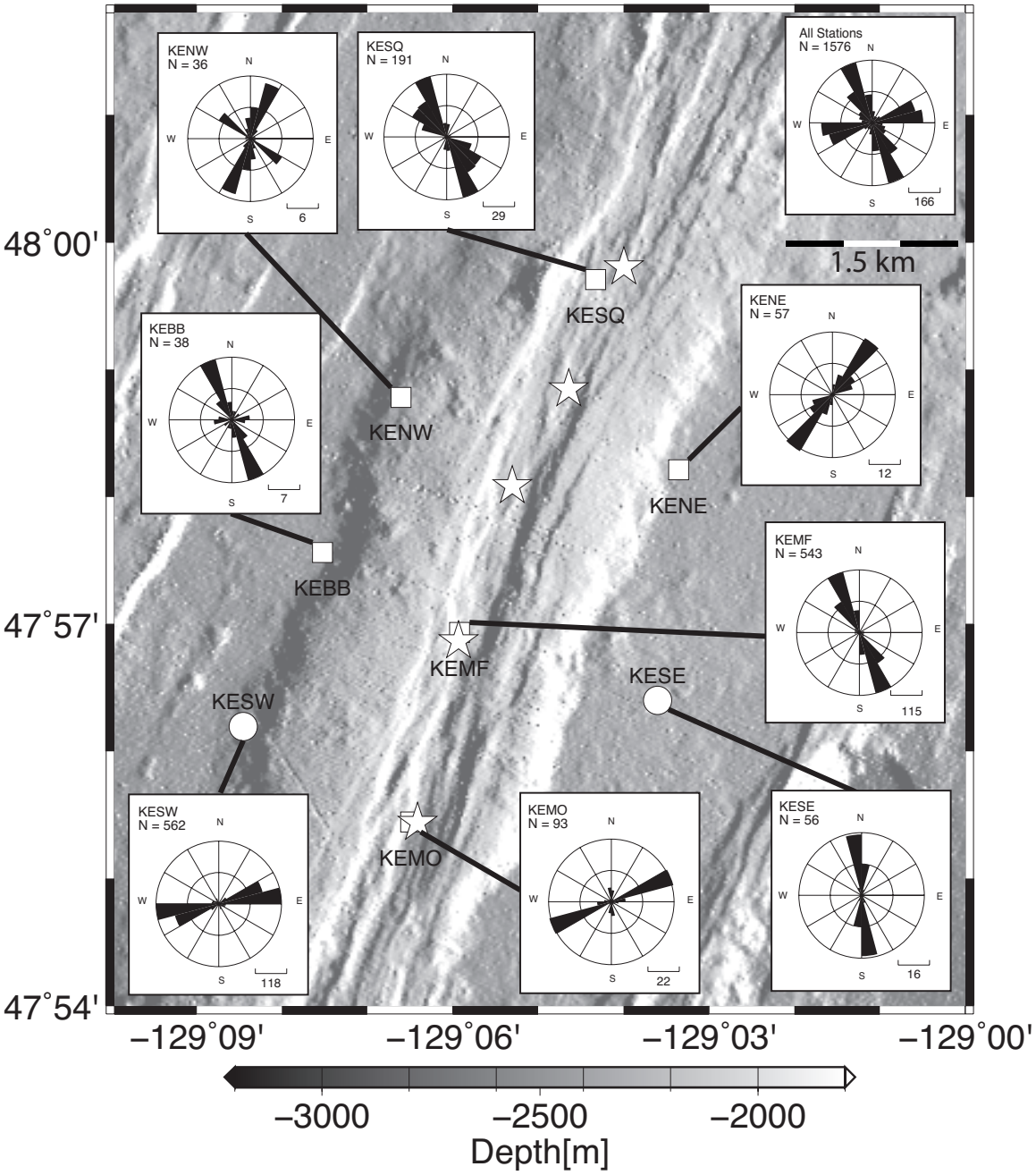

Figure 5. Rose diagrams of each OBS station and all stations. The number of events is listed in the upper left corner in each box as N and the scale of bins are shown in the lower right corner. The trend of all stations points to the north-west direction. Fast polarization directions at stations KEMF, KESQ, KENE, KEBB, KESE, and KESW show clear trends while bimodal trends are obtained at station KENW, and KEMO.

Numerous earthquakes were recorded at station KEMF. Figure 6 shows equal area projections of fast polarization directions, which are useful to investigate variations by back azimuth and incident angle (e.g. Munson et al., 1995; Vlahovic et al., 2003; Peng and Ben-Zion, 2004; Elkibbi and Rial, 2005). The fast polarization directions show a clear NW trend at shallow depths though the trend does not depend on back azimuths (Figure 6a). At deeper depths, shear wave splitting is measured at events primarily from the north (Figure 6b) and also shows a similar trend for the fast polarization directions.

At station KEMF, a clear directional dependence of the magnitude of δt may be present (Figure 7a); however, this correlation is not evident for earthquakes below 2.5 km depth (Figure 7b). At shallow depths (<2.5km), shear wave splitting coming from the north yields delay times of about ~0.1 s (dashed ellipsoid in Figures 7a) while shear wave splitting coming from the south yields delay times of about 0.05 s (solid ellipsoid in Figure 7a). For earthquakes with deeper depths (Figure 7b), the 0.05 s delay from shear waves from the south is not evident. Delay times and earthquake depths at station KEMF are shown in Figure 8. There is no clear correlation of delay time with hypocentral depth. This suggests that variations in splitting delay times are independent of depth but that they may vary laterally. From this we infer that the structure giving rise to anisotropy is concentrated within the shallow crust and that shallow crustal anisotropy is laterally variable.

Figure 6 (next page). Equal area projections of fast polarization directions out to 20˚ at station KEMF. a) For hypocenters shallower than the depth of the AMC (0 - 2.5 km depths.) (b) For hypocenters deeper than the depths of AMC (2.5 - 6.0 km depths.) Lines indicate fast polarization directions. The locations of the center of the lines are defined by back azimuths and incident angles. Incident angles are shown as distances from the center of the circle to the center of the lines. Incident angles are determined by ray parameters using TauP (Crotwell et al., 1999).

a)

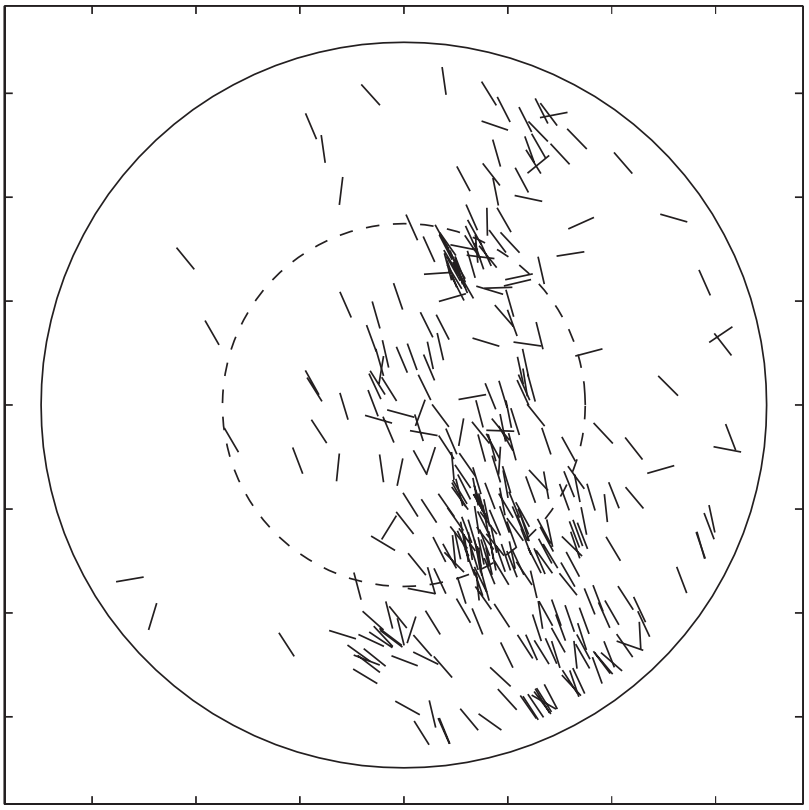

b)

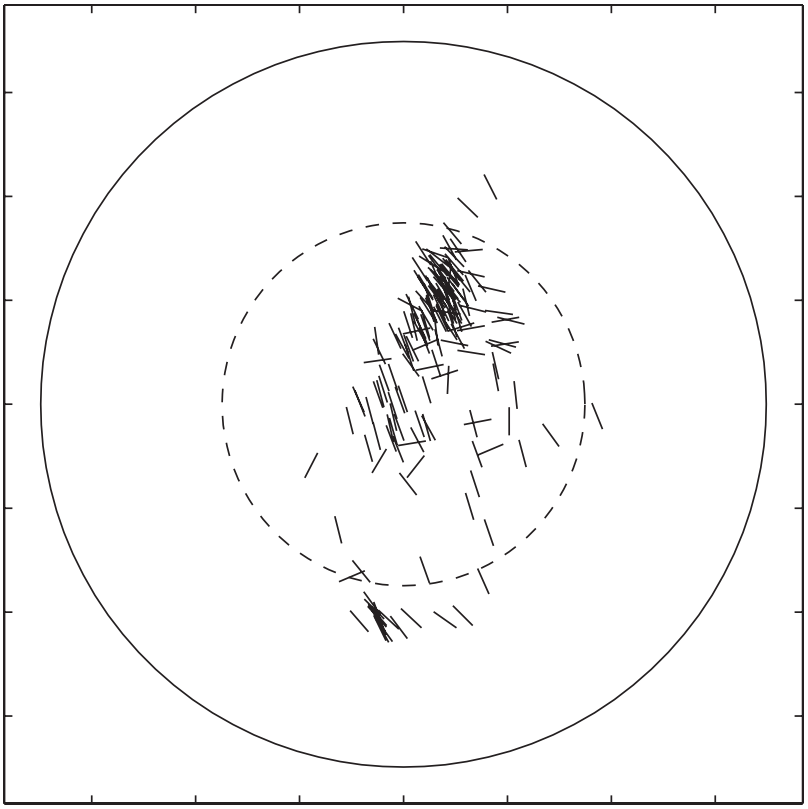

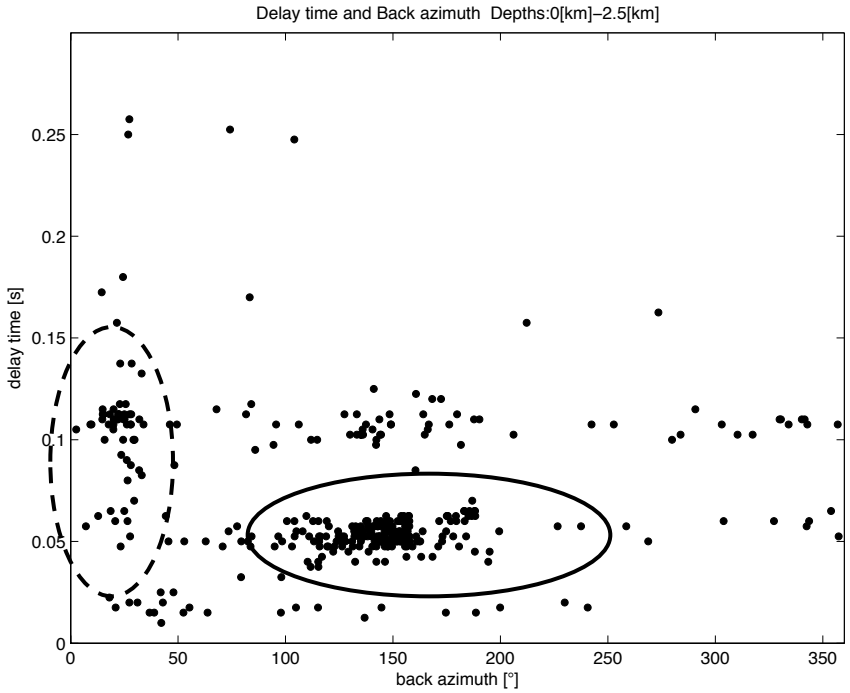

a)

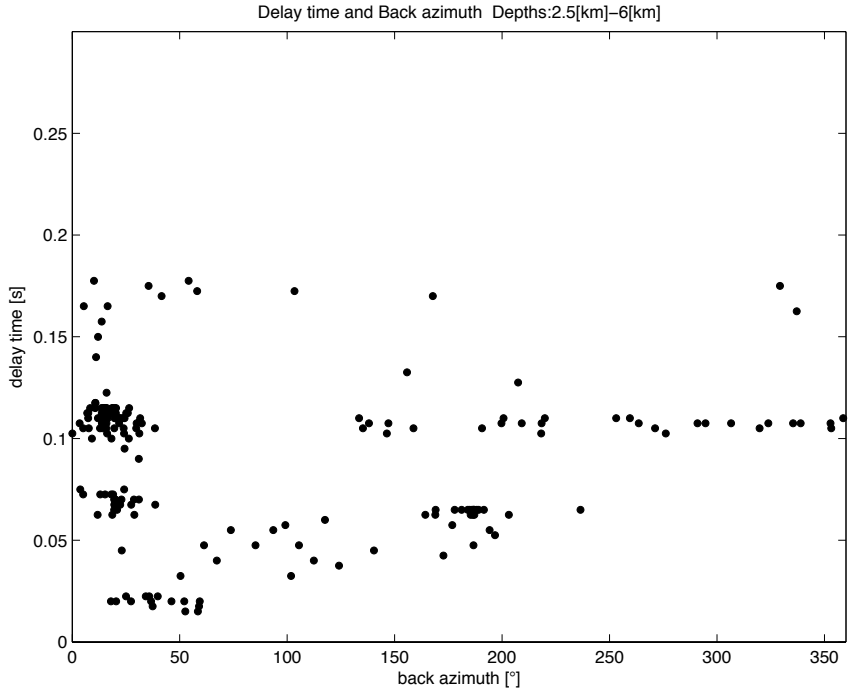

b)

Figure 7. Back azimuths and δt for station KEMF. a) 0 - 2.5 km depths. Delay times may have a directional dependence (dashed and solid circles). b) 2.5 - 6.0 km depths.

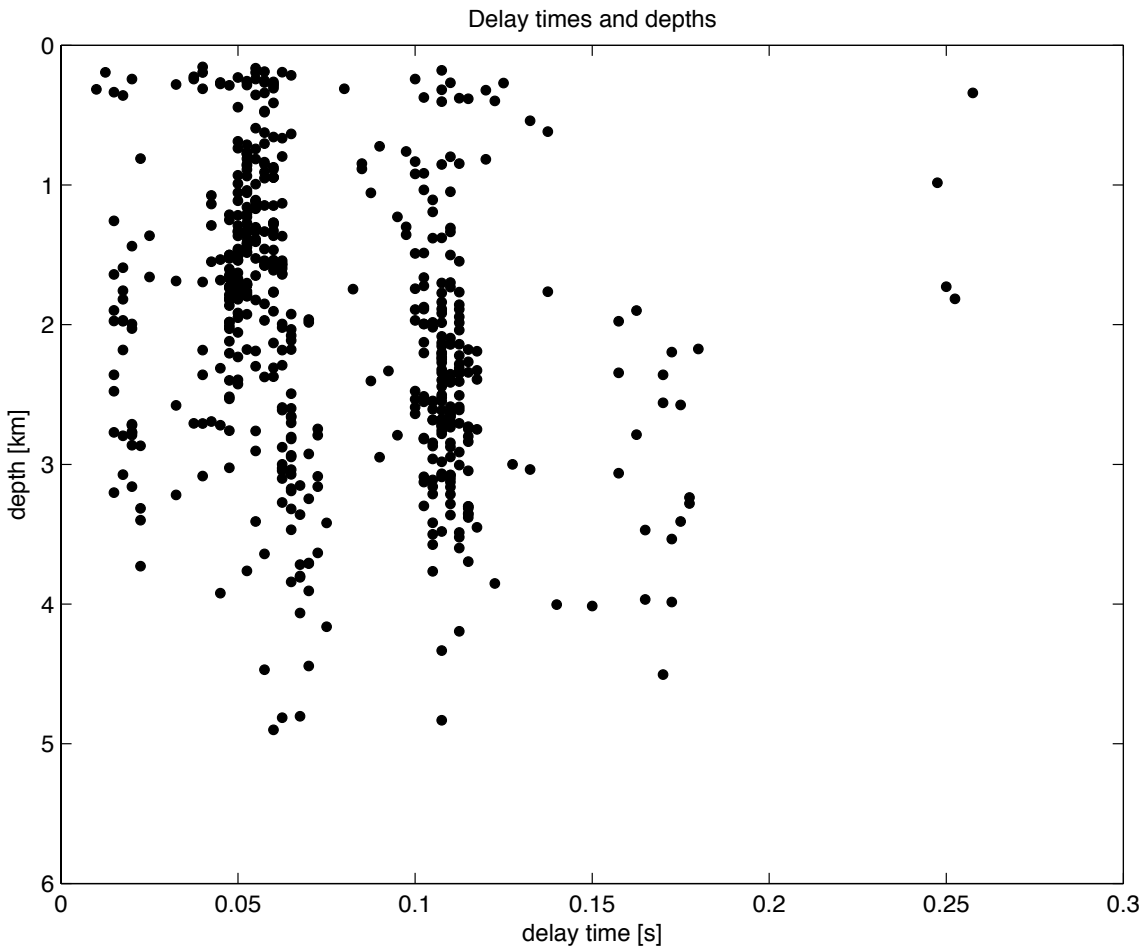

Figure 8. Delay times and depths from 0 to 2.5 km at station KEMF.

Figure 9 shows fast polarization directions and delay times by date for station KEMF. For both deep and shallow hypocenters the fast polarization directions do not vary with time. The split times show two trends, with delay times of 0.05 and 0.1 s being most common. This bimodal distribution of delay times is independent of earthquake depth. We attribute this bimodal distribution of splitting times to imprecision in the method. In particular, the error surfaces, which are a function of splitting direction and delay time, tend to have ripples along the delay-time axis and thus several local minima. We conclude that the fast directions and delay times do not significantly change during the time of our experiment.

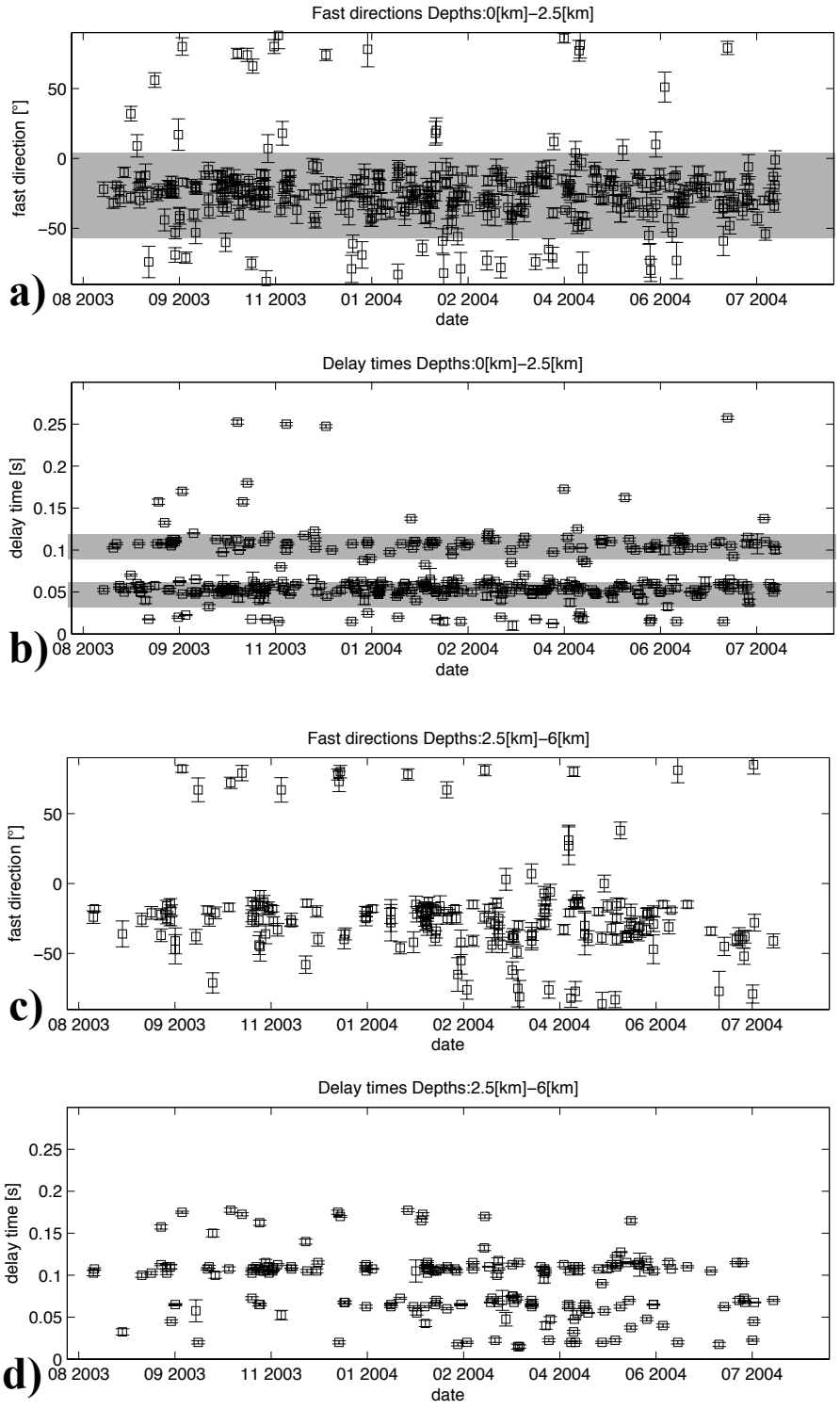

Figure 9. Plots of fast polarization directions and delay times at station KEMF: a) Fast polarization directions at depths of 0 - 2.5 km. The NW trend is shown as a shadowed box. b) Delay times at depths of 0 - 2.5 km. Direction and delay times are constant through time (two shadow boxes). c) Fast polarization directions at depths of 2.5 - 6.0 km. d) Delay times at depths of 2.5 - 6.0 km.

At station KEMO we do observe a directional dependence of the fast polarization direction (Figures 10a, 10b). Events that locate north and south of this station show different fast polarization directions (the solid circles in Figure 10b). Fast polarization directions for waves arriving from the north are more scattered while fast polarization directions from the south closer to N60˚E. Delay times of events from the north are also more scattered (Figure 11). We infer that the anisotropic structure is more complicated between the Main Endeavour field and the Mothra vent fields.

At stations KESQ and KEBB we observed fast polarization directions aligned in the northwest direction. The stations are located on the ridge axis and on the flank of the axial valley, respectively. The shear wave splitting at stations KESQ and KEBB does not show variation with back azimuth (Figures 12, 13). Many of the earthquakes observed at these stations were located beneath the Main Endeavour field, thus fast polarization directions for both of these stations are likely to reflect the anisotropic structure beneath either Main Endeavour, High Rise or Salty Dawg vent fields. The counterclockwise rotation of fast polarization directions relative to the ridge axis is consistent with the trend observed at station KEMF, although the directions are not identical. Figure 13 shows fast polarization directions and delay times plotted by date for stations KESQ and KEBB. Delay times stay fairly constant through time at stations KESQ and KEBB. Fast polarization directions at both of the stations point to the northwest, although station KEBB shows more a consistent value of fast polarization than station KESQ. We note that the fast polarization directions and delay times do not change significantly with time.

a)

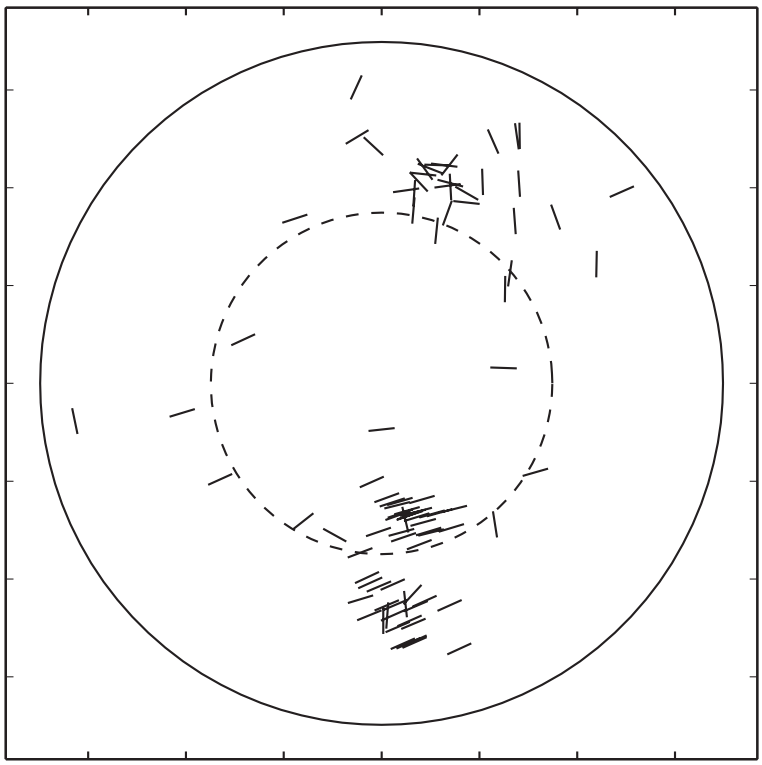

b)

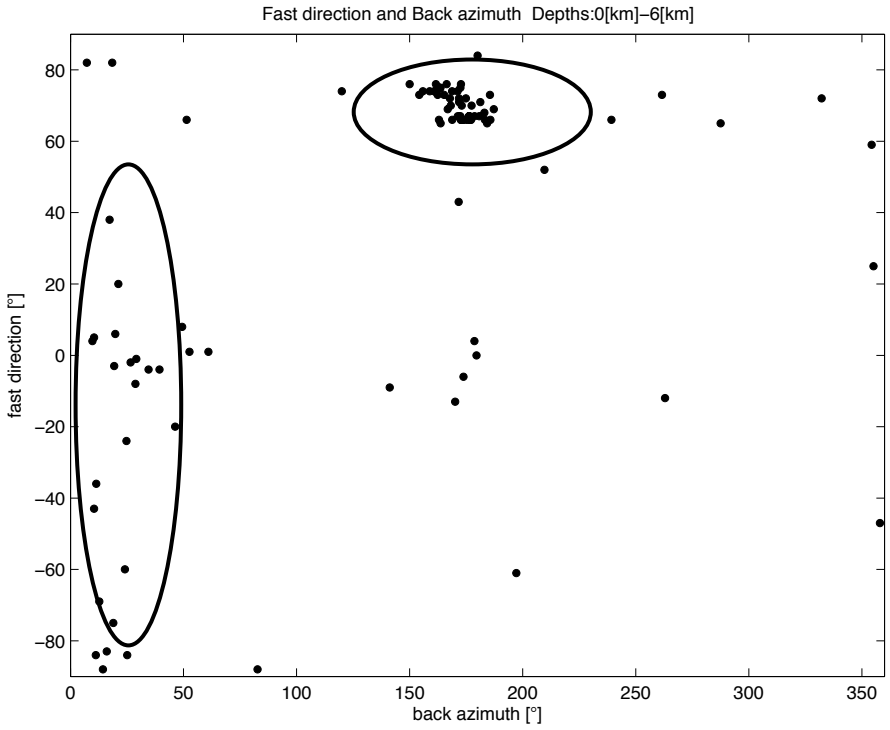

Figure 10. Directional dependence of fast polarization directions at station KEMO. a) An equal area projection of fast polarization directions out to 20˚ beneath station KEMO. b) Fast polarization directions and back azimuths. The trends of delay time depend on back azimuths (solid circles).

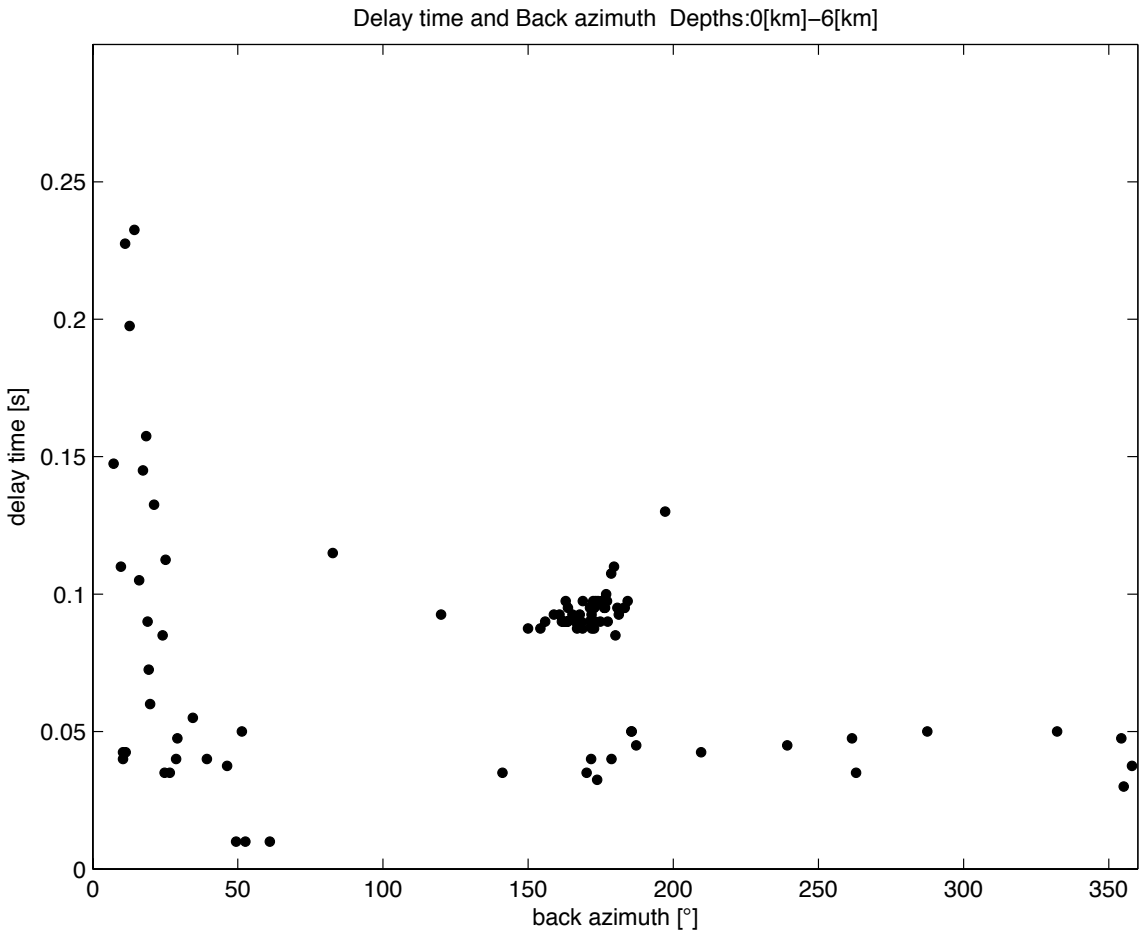

Figure 11. Delay times and back azimuths at depths of 0 - 2.5 km at station KEMO.

a)

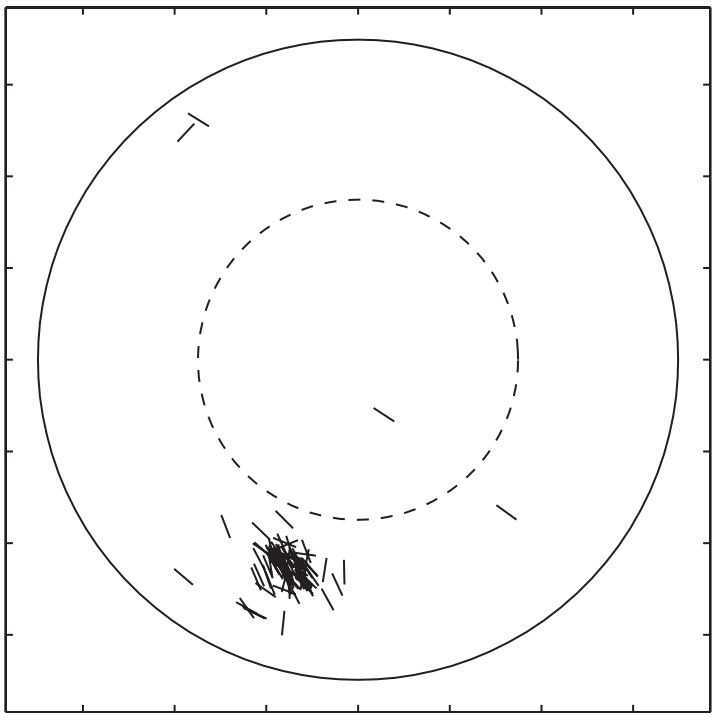

b)

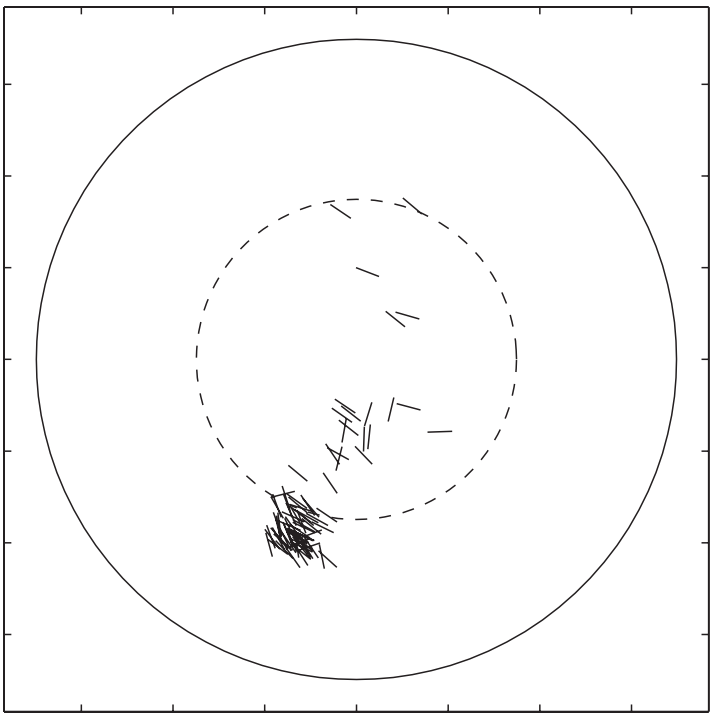

Figure 12. Equal area projections of fast polarization directions out to 20˚ beneath stations KESQ and KEBB. (a) 0 - 2.5 km depths at station KESQ. (b) 2.5 - 6.0 km depths at station KESQ. (c) 0 - 2.5 km depths at station KEBB. (d) 2.5 - 6.0 km depths at station KEBB.

c)

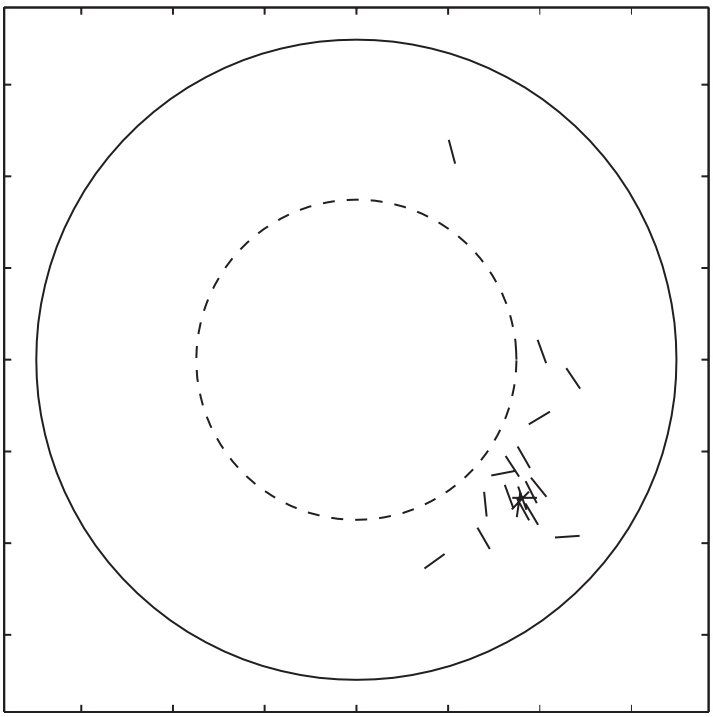

d)

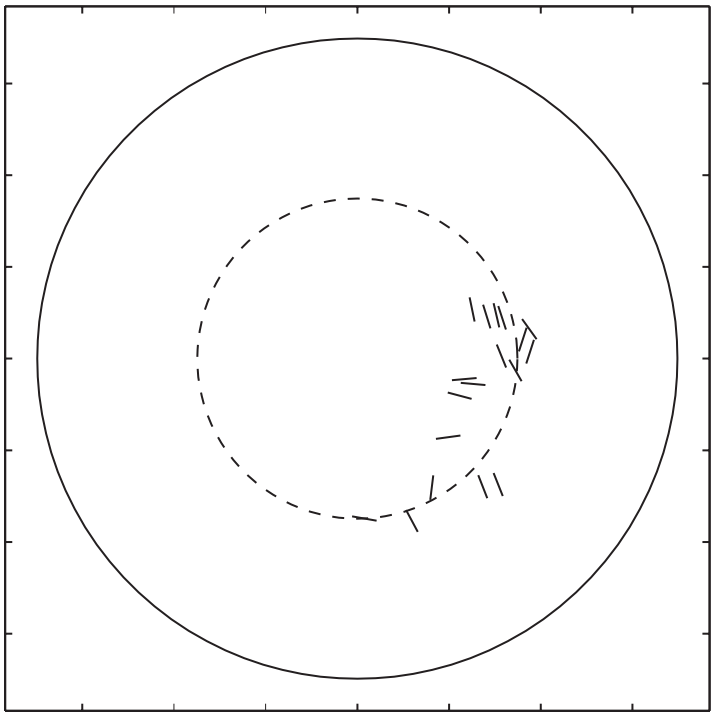

Figure 12. (continued)

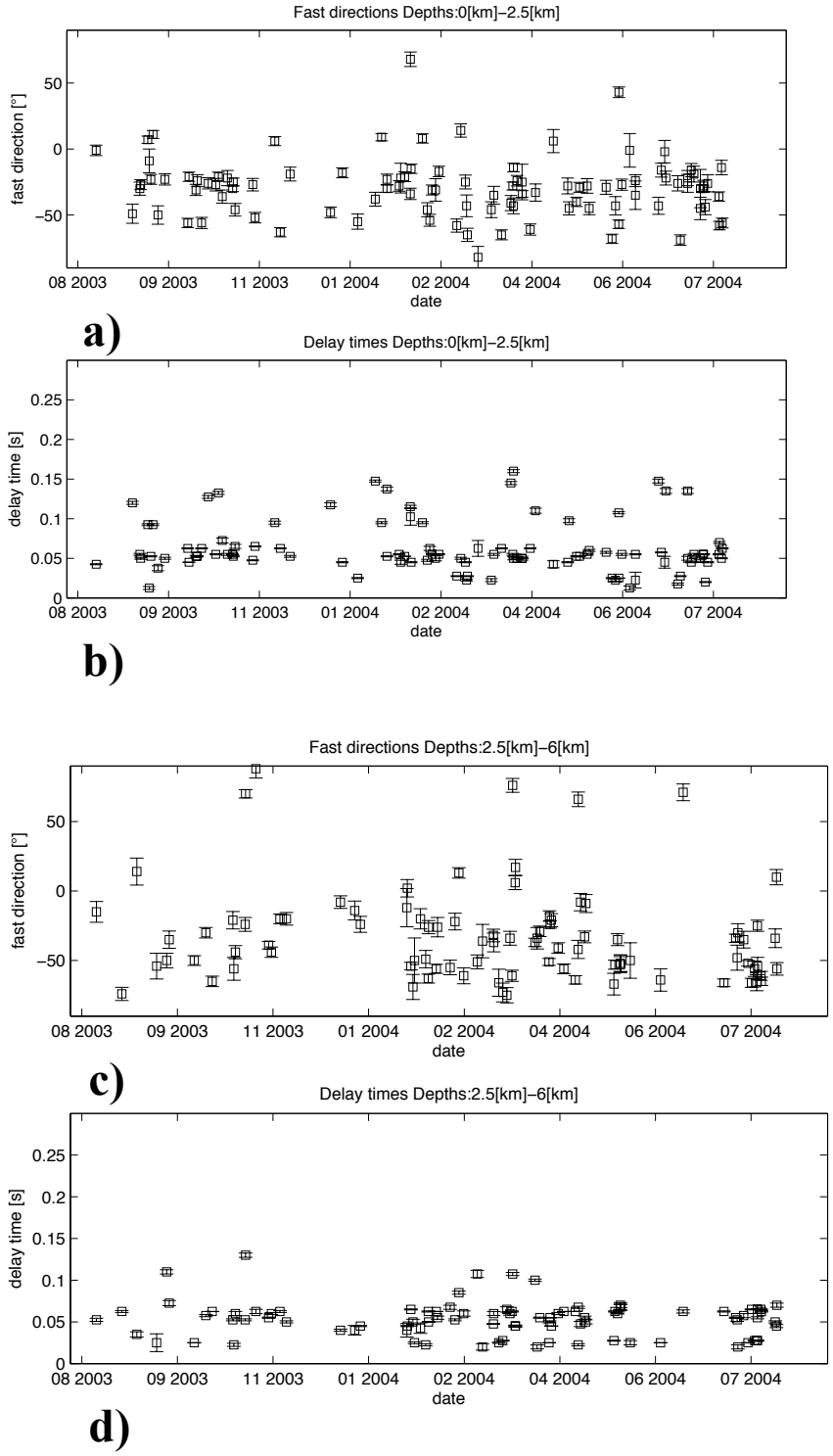

Figure 13. Splitting parameters versus date at stations KESQ and KEBB. Data at station KESQ are shown in (a - d) and data at station KEBB are shown in (e-h). Fast polarization directions are shown in a) and e) at depths of 0 - 2.5 km and in c) and g) at depths of 0 - 2.5 km. Delay times are shown in b) and f) at depths of 0 - 2.5km and in d) and h) at depths of 2.5 - 6.0 km.

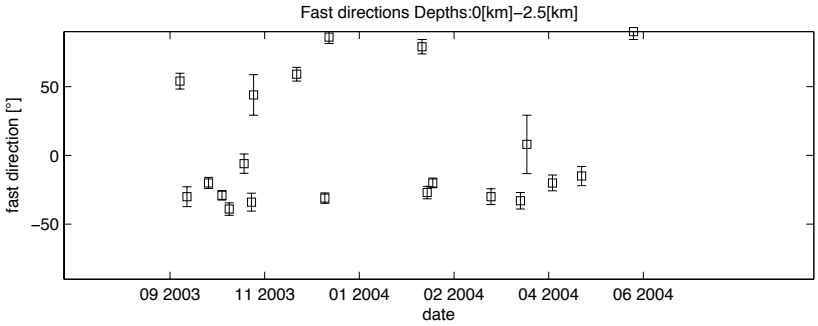

e)

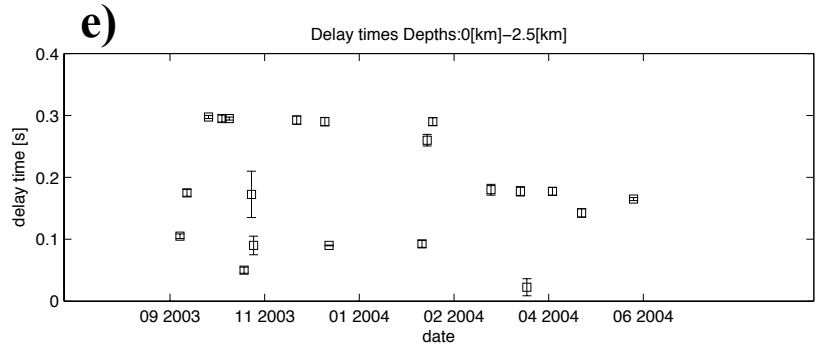

f)

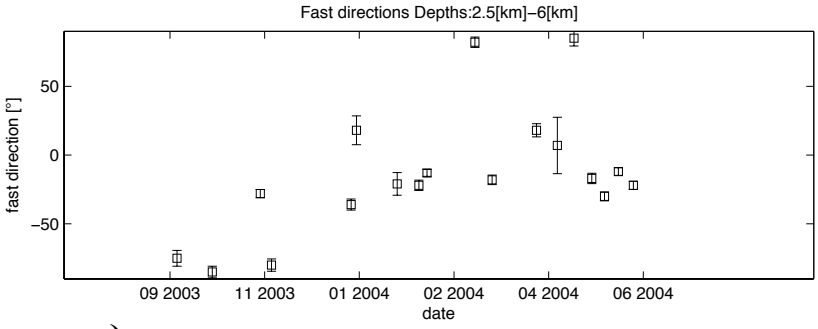

g)

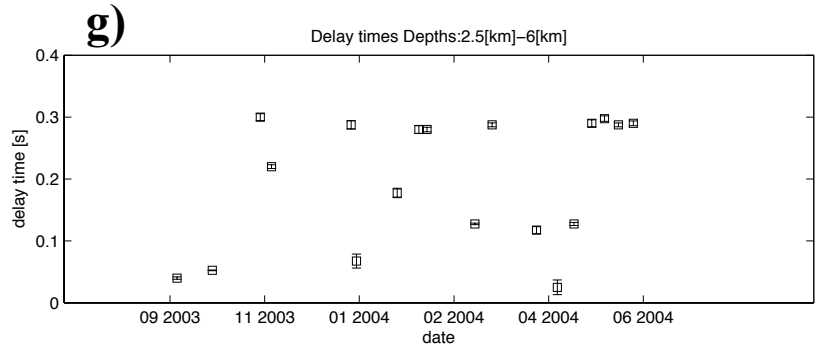

h)

Figure 13. (continued)

Fast polarization directions at stations KENW, KENE, KESE and KESW are consistent at each station but vary significantly between stations (Figure 14). Most of the observed events occur near the Main Endeavour vent field as well as beneath station KEBB and KESQ. On the basis of our results, station KENW is likely to be located above an unclear anisotropic area since the number of successful measurements is low (51) and the fast polarization directions have a bimodal distributions (Figures 5, 14a). Station KENE records earthquakes with back-azimuths mainly from the southwest directions; however, fast polarization directions measured for events from different directions are generally consistent (Figure 14b). Station KESE is a "seismonument" and the data quality is less than the other stations, but results of events from the west show a clear trend of fast polarization directions to the north (Figure 14c). Station KESW is also a "seismonument" and fast polarization directions are fairly consistent with the results around station KEMO (Figure 14d).

Following the first year of the deployment, seismic data is available at stations KENW, KENE, KESE, and KESW. KESQ has limited number of measurable events in the third year. Fast polarization directions plotted by date and rose diagrams at the stations, except for the station KESQ, are shown in Figure 15. We do not observe any temporal changes in the fast polarization directions. Table 3 compares the fast polarization directions until August 2006.

	Period 1			Period 2 (EQ swarm)			Period 3		
	ϕ(deg)	R	±ϕ(deg)	ϕ(deg)	R	±ϕ(deg)	ϕ(deg)	R	±ϕ(deg)
KESQ	-32.94	0.89	1.99	-	-	-	-29.89	0.66	10.36
KENW	-5.73	0.82	5.00	17.74	0.73	8.68	1.34	0.57	17.10
KENE	35.99	0.91	2.90	42.66	0.98	3.32	39.21	0.94	4.49
KESE	-9.88	0.93	2.41	-2.37	0.94	3.68	-	-	-
KESW	63.61	0.70	1.82	64.51	0.78	4.71	31.23	0.65	8.02
KEBB	4.70	0.66	8.77	14.65	0.73	11.67	-	-	-

Table 3. Mean fast polarization directions for each deployment period. Mean of fast polarization directions and their standard errors are derived by Davis (2002). Period 1 starts from the beginning of the deployment of the Keck seismic network to 15, February 2005. Period 2 (15, February 2005 – 15, March 2005) is intended to cover the period of the February 2005 earthquake swarm. Period 3 starts after 15, March 2005 until the end of the availability of each OBS station.

a)

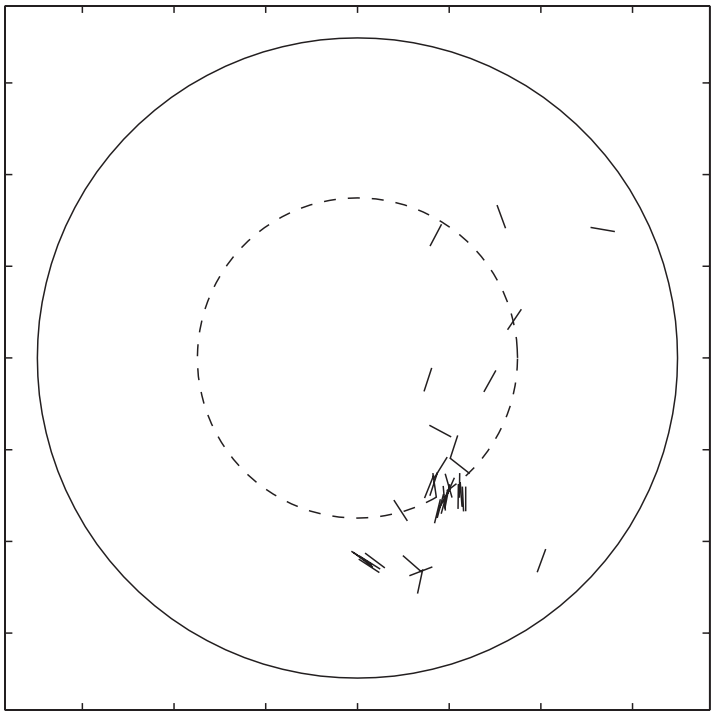

b)

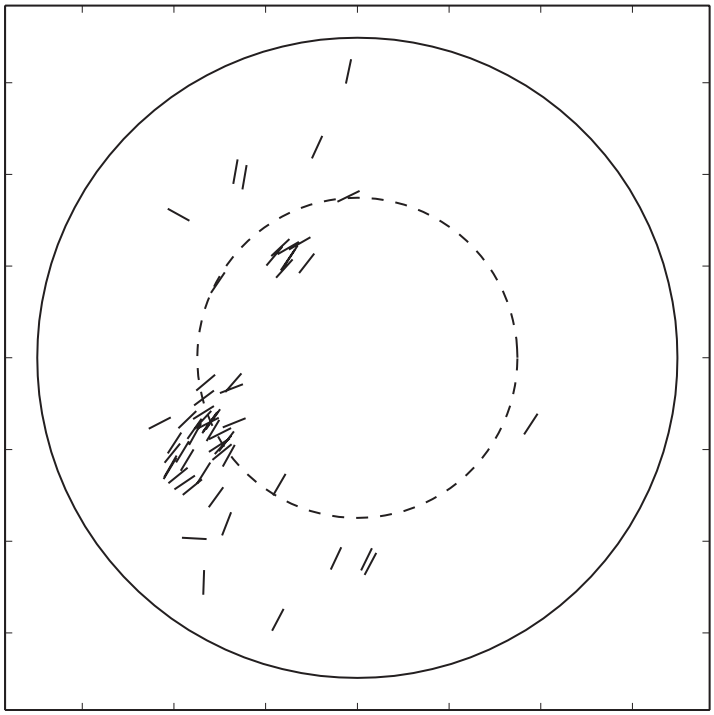

Figure 14. Equal area projections of fast polarization directions out to 20˚ beneath stations KENW, KENE, KESE, and KESW. Events depths are until 6.0 km. (a) station KENW, (b) station KENE, (c) station KESE, (d) station KESW.

c)

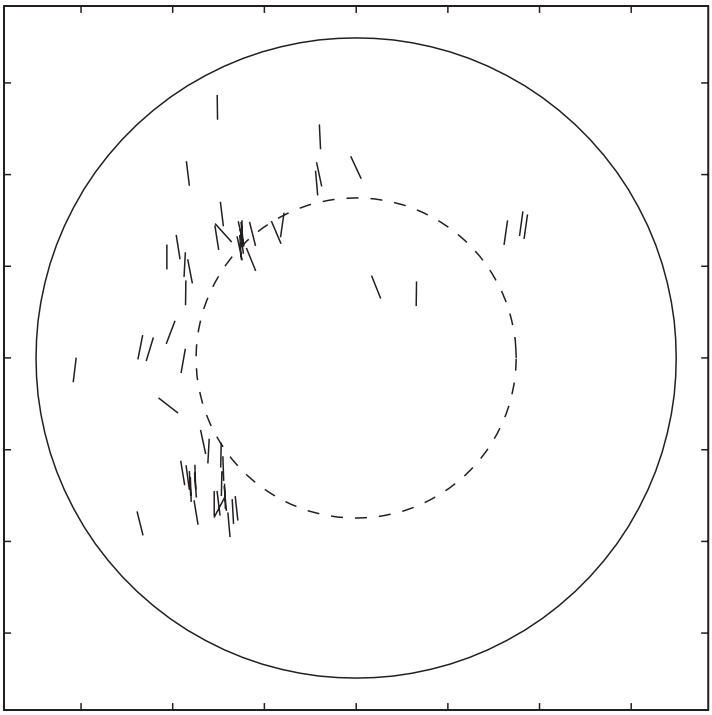

e)

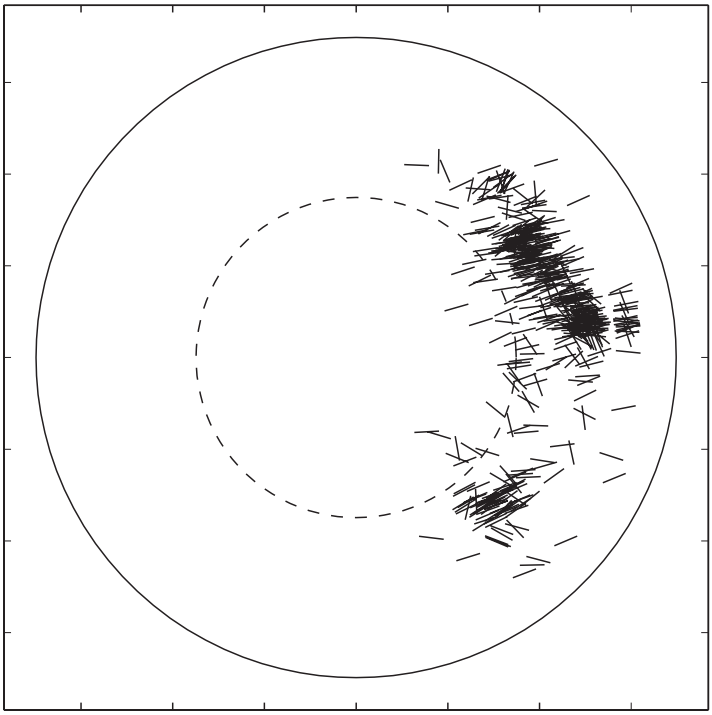

Figure 14. (continued)

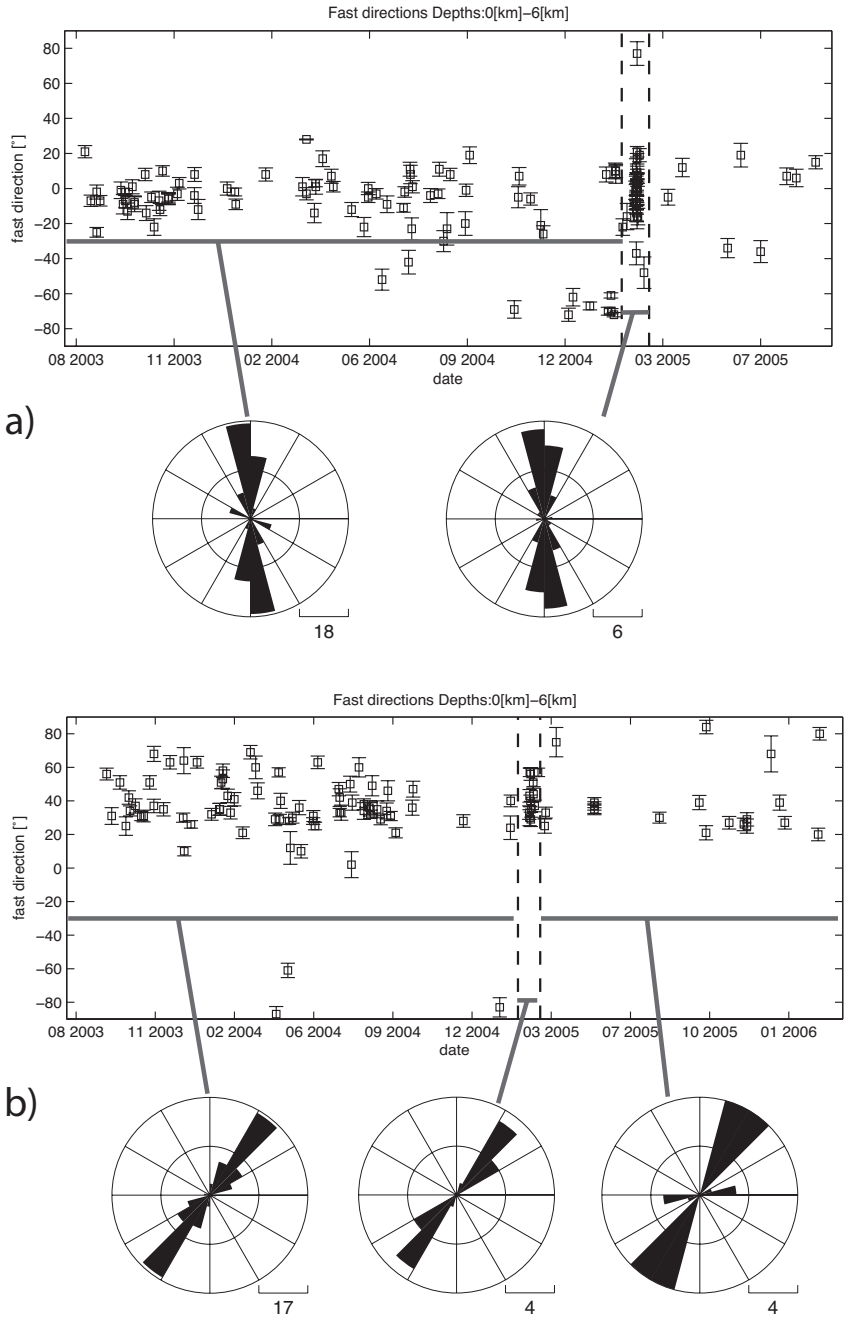

Figure 15. Fast polarization directions at stations KESE, KENE, KESW, and KENW. Each figure show individual stations: a) station KESE, b) station KENE, c) station KESW, and d) station KENW. Fast polarization directions plotted by date. Two dashed lines indicate 15, February 2005 and 15, March 2005. Rose diagrams are showing fast polarization directions prior to 15, February 2005, fast polarization directions from 15, February 2005 to 15, March 2005, and fast polarization directions after 15, March 2005. We do not show the rose diagram of fast polarization directions at station KESE after 15, March 2005 because of small number of measurement results.

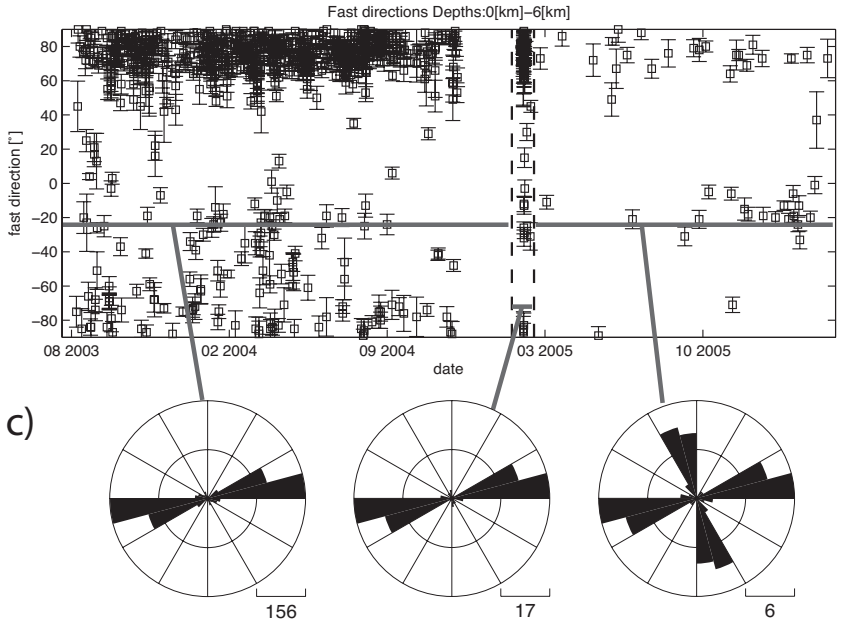

c)

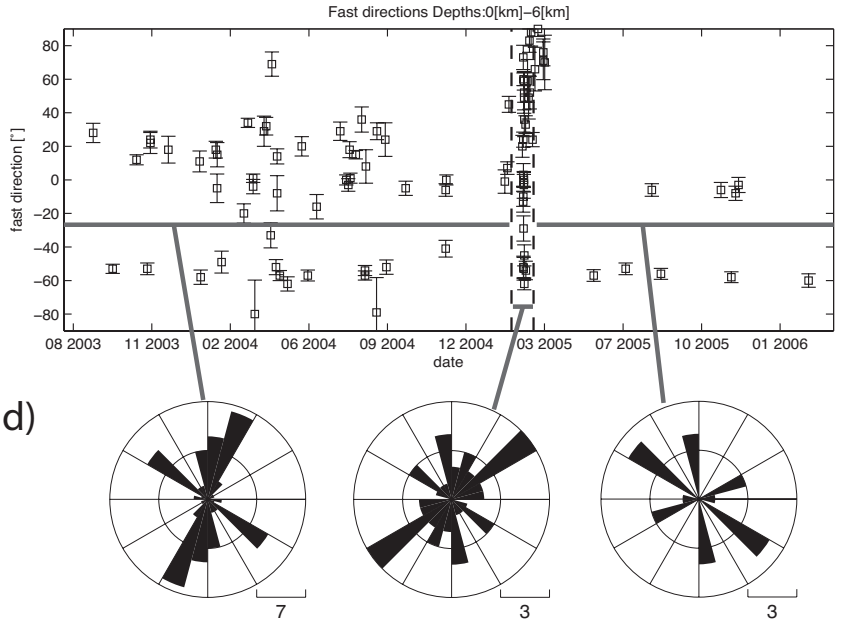

d)

Figure 15. (continued)

CHAPTER V

DISCUSSION

Our results indicate that near the center of the Endeavour segment the fast-directions of shear wave splitting are not consistently ridge parallel, but instead vary significantly between stations. We note that measurements at individual stations show clear trends in fast polarization directions. Delay times at each station are also generally consistent, though in some cases individual stations report a bimodal distribution of delay times that we attribute to imprecision in the methodology. The splitting times do not correlate with earthquake depth. These results may indicate the source of anisotropy is restricted to shallow depths (e.g. Barclay and Toomey, 2003). We do not observe temporal variation in splitting parameters. Taken as a whole, the splitting times vary from 0.05 to 0.3 s at many stations, irrespective of the difference in fast polarization directions. The larger delay times may be explained by the existence of highly fractured crust at shallow depths.

The directional dependence of delay times at station KEMF is consistent with the hypothesis that crustal anisotropy is laterally variable. The largest number of events occurs near the Main Endeavour field and there is a clear trend of N30˚W. The consistent fast polarization directions with different delay times at station KEMF may be due to spatial variations in the magnitude of crustal anisotropy. Alternatively, the variations in delay time may be the result of imprecision in the methodology.

Inter-station differences in shear wave splitting may be caused by heterogeneity in anisotropic structure around the Main Endeavour vent field. For example, at station

KEMO (Figures 5, 10b, and 11) one clear trend of N60˚E is obtained for events to the south. The events from the north that have scattered anisotropy at station KEMO have a similar trend as the events at station KEMF. Both directions of anisotropy may result from changes in shallow crustal anisotropic structures around the Main Endeavour vent field. The trend of N60˚E at station KEMO is consistent with the trend of station KESW (Figure 5). The anisotropy observed at station KESW is to the west of the station and the location is not strictly consistent with the anisotropy around KEMO (Figures 10a, and 14d). Trends of fast polarization directions at station KEBB are similar to the results at station KEMF, though the delay times (~ 0.3 s) at station KEBB are longer than the results at station KEMF (0.05 – 0.1 s). Shear wave splitting measured at station KESQ also has the similar fast polarization directions with station KEMF. The events measured at station KESQ come from the Main Endeavour, High Rise, and Salty Dawg and Sasquatch vent fields.

The observed variation in seismic anisotropy is not consistent with the regional extensional stresses as one would expect for the Endeavour Segment. The variation in fast polarization directions may be caused by many factors, intersecting crack distributions (Liu et al., 1993), dipping cracks, or multiple fracture sets (Liu et al., 2006). The bimodal distribution of fast polarization directions, for example at stations KENW and KEMO can be caused by dipping cracks. Almendros et al. (2000) also measured shear wave splitting close to station KEMF. While the number of measurements is limited, they also obtain fast polarization directions that are not parallel to the ridge axis. We note that the faults and fissures trend ~N25˚W in the vicinity of station KEMF

(Delaney et al., 1992). However, the results at stations KENW, KEMO, and KEMF do not have a trend of ridge parallel faults and fissures.

We did not observe a clear temporal change in splitting parameters during three years deployment period, except for station KENW. Although a regional-scale change in the stress field is likely to have occurred due to a seismic swarm that was located primarily to the north of our array (Hooft et al., 2010), the fast polarization directions do not change at OBS stations near the center of the Endeavour Segment. From the consistency of fast polarization directions through time and inter-station variability in fast directions, we infer that the source of stress causing seismic anisotropy near the center of the Endeavour Segment is no related to regional-scale processes, but instead reflects the state of stress near the hydrothermal system.

The deviation of fast polarization directions from the ridge-parallel direction is likely to result from stress perturbations caused by magmatic or hydrothermal processes. The sources of stresses at the Endeavour Segment include tectonic extension, magmatic inflation and diking, and variations in pore pressures resulting from heat transfer and/or fluid flow. Clear ridge-parallel faults are observed in the surface of geology (Delaney et al., 1992; Wilcock et al., 2002) and near the vent fields the faults and fissures also strike almost parallel to the ridge-axis (Glickson et al., 2007). Inter-station differences in fast polarization directions are not consistent with these geologic sources of seismic anisotropy. We presume that the observed variability in splitting parameters is caused by local variations in stress that are related to magmatic and hydrothermal processes.

We postulate that the anisotropy above the axial magma chamber may be affecting the hydrogeological structure. Variations in fast polarization directions at station KEMO indicates that different stress fields exist in the Main Endeavour field and the Mothra vent field. It is qualitatively consistent with the focused flow around the Main Endeavour field and the diffuse type vents in the Mothra or Sasquatch vent fields. Changes in fast polarization directions by 90˚ have been observed near seismogenic faults (e.g. Crampin et al., 2002; Padhy and Crampin 2006). The variety of fast polarization directions is consistent with the complex stress fields in the area and spatial variation in hydrothermal processes around vent fields may contribute to scatter in our results.

CHAPTER VI

CONCLUSION

We measured shear wave splitting on data recorded by an ocean-bottom seismic array deployed near the center of the Endeavour Segment. We used an automated method that employs a clustering technique. The methodology eliminates noisy data by using a combination of criteria. We focus on measurements for earthquakes with depths less than 6.0 km. The inter-station variability in fast polarization directions is large. We also investigate the temporal change of fast polarization directions and only one station shows evidence for temporal variations in the fast polarization directions. Since our deployment periods include an earthquake swam that occurred in February 2005, we assume that the earthquake swarm does not affect the regional stress field and the heterogeneous anisotropic structure near the segment's center is most likely caused by other factors. The inconsistency of fast polarizations across OBS stations may reflect a complex upper crustal structure and the variation of stress field in the vicinity of the hydrothermal vent fields. Heterogeneous fast polarization directions may indicate that the anisotropy in the middle of the Endeavour Segment is affected by stress perturbations related to segment center magmatic and/or hydrothermal processes.

REFERENCES CITED

Almendros, J., A. H. Barclay, W. S. D. Wilcock, and G. M. Purdy (2000), Seismic anisotropy of the shallow crust at the Juan de Fuca Ridge, *Geophysical Research Letters*, *27*(19), 3109-3112.

Barclay, A. H., and D. R. Toomey (2003), Shear wave splitting and crustal anisotropy at the Mid-Atlantic Ridge, 35 N, *J. Geophys. Res*, *108*(B8), 2378.

Carbotte, S. M., R. S. Detrick, A. Harding, J. P. Canales, J. Babcock, G. Kent, E. Van Ark, M. Nedimovic, and J. Diebold (2006), Rift topography linked to magmatism at the intermediate spreading Juan de Fuca Ridge, *Geology*, *34*(3), 209, doi:10.113/G21969.1.

Crampin, S., A. Gudmundsson, and R. Stefánsson (2002), Indication of high pore-fluid pressures in a seismically-active fault zone, *Geophysical Journal International*, *151*(2), F1–F5.

Crotwell, H. P., T. J. Owens, and J. Ritsema (1999), The TauP Toolkit: flexible seismic travel-time and ray-path utilities, *Seismological Resarch Letters*, *70*, 154-160.

Davis, J. C. (2002), *Statistics and Data Analysis in Geology Third Edition*, John Wiley.

DeMets, C., R. G. Gordon, D. F. Argus, and S. Stein (1994), Effect of recent revisions to the geomagnetic reversal time scale on estimates of current plate motions, *Geophysical Research Letters*, *21*(20), 2191, doi:10.1029/94GL02118.

Delaney, J. R., V. Robigou, R. E. McDuff, and M. K. Tivey (1992), Geology of a Vigorous Hydrothermal System on the Endeavour segment, Juan de Fuca Ridge, *Journal of geophysical research*, *97*(B13), 19663–19.

Elkibbi, M., and J. a. Rial (2005), The Geysers geothermal field: results from shear-wave splitting analysis in a fractured reservoir, *Geophysical Journal International*, *162*(3), 1024-1035, doi:10.1111/j.1365-246X.2005.02698.x.

Gerst, A., and M. K. Savage (2004), Seismic anisotropy beneath Ruapehu volcano: a possible eruption forecasting tool, *Science*, *306*(5701), 1543.

Glickson, D. a., D. S. Kelley, and J. R. Delaney (2007), Geology and hydrothermal evolution of the Mothra Hydrothermal Field, Endeavour Segment, Juan de Fuca Ridge, *Geochemistry Geophysics Geosystems*, *8*(6), doi:10.1029/2007GC001588.

Hooft, E. E. E. et al. (2010), A seismic swarm and regional hydrothermal and hydrologic perturbations: The northern Endeavour segment, February 2005, *Geochemistry Geophysics Geosystems*, *11*(12), 1-23, doi:10.1029/2010GC003264.

Liu, E., M. Chapman, Z. Zhang, and J. Queen (2006), Frequency-dependent anisotropy: Effects of multiple fracture sets on shear-wave polarizations, *Wave Motion*, *44*(1), 44-57, doi:10.1016/j.wavemoti.2006.06.006.

Liu, E., S. Crampin, and J. Queen (1993), Behaviour of shear waves in rocks with two sets of parallel cracks, *Geophysical Journal*, *113*(2), 509-517, doi:10.1111/j.1365-246X.1993.tb00903.x.

Marson-Pidgeon, K., and M. K. Savage (1997), Frequency-dependent anistropy in Wellington, New Zealand, *Geophysical Research Letters*, *24*(24), 3297–3300.

McClain, J., M. Begnaud, M. Wright, J. Fondrk, and G. Von Damm (1993), SEISMICITY AND TREMOR IN A SUBMARINE HYDROTHERMAL FIELD:THE NORTHERN JUAN DE FUCA RIDGE, *Geophysical research letters*, *20*(17), 1883–1886.

Munson, C., C. Thurber, and Y. Li (1995), Crustal shear wave anisotropy in southern Hawaii : Spatial and temporal analysis, *Journal of Geophysical Research*, *100*(B10), 367-377.

Padhy, S., and S. Crampin (2006), High pore-fluid pressures at Bhuj, inferred from 90 degrees-flips in shear-wave polarizations, *Geophysical Journal International*, *164*(2), 370-376.

Peng, Z., and Y. Ben-Zion (2004), Systematic analysis of crustal anisotropy along the Karadere–Düzce branch of the North Anatolian fault, *Geophysical Journal International*, *159*(1), 253-274, doi:10.1111/j.1365-246X.2004.02379.x.

Roman, D. C., M. K. Savage, R. Arnold, J. L. Latchman, and S. De Angelis (2011), Analysis and forward modeling of seismic anisotropy during the ongoing eruption of the Soufrière Hills Volcano , Montserrat, 1996-2007, *Journal of Geophysical Research*, *116*(B3), B03201, doi:10.1029/2010JB007667.

Savage, M. (1999), Seismic anisotropy and mantle deformation: what have we learned from shear wave splitting, *Reviews of Geophysics*, *37*(1), 65–106.

Savage, M. K., A. Wessel, N. A. Teanby, and A. W. Hurst (2010), Automatic measurement of shear wave splitting and applications to time varying anisotropy at Mount Ruapehu volcano, New Zealand, *Journal of Geophysical Research*, *115*(B12), 1-17, doi:10.1029/2010JB007722.

Silver, P. G., and W. W. Chan (1991), SHEAR-WAVE SPLITTING AND SUBCONTINENTAL MANTLE DEFORMATION, *Journal of Geophysical Research*, *96*(B10), 16429-16454.

Stakes, D., J. McClain, T. VanZandt, P. McGill, and M. Begnaud (1998), Corehole seismometer development for low-noise seismic data in a longsterm seafloor observatory, *Journal of Geophysical Research*, *25*(14), 2745-2748.

Teanby, N. A., J. M. Kendall, and M. Van Der Baan (2004), Automation of shear-wave splitting measurements using cluster analysis, *Bulletin of the Seismological Society of America*, *94*(2), 453-463.

Van Ark, E. M., R. S. Detrick, J. P. Canales, S. Carbotte, A. Harding, G. Kent, M. Nedimovic, W. Wilcock, J. Diebold, and J. Babcock (2007), Seismic structure of the Endeavour Segment, Juan de Fuca Ridge: Correlations with seismicity and hydrothermal activity, *Journal of Geophysical Research*, *112*(B2), B02401.

Vlahovic, G., M. Elkibbi, and J. . Rial (2003), Shear-wave splitting and reservoir crack characterization: the Coso geothermal field, *Journal of Volcanology and Geothermal Research*, *120*(1-2), 123-140, doi:10.1016/S0377-0273(02)00368-2.

Wilcock, W. S. D., E. E. E. Hooft, D. R. Toomey, P. R. McGill, A. H. Barclay, D. S. Stakes, and T. M. Ramirez (2009), The role of magma injection in localizing black-smoker activity, *Nature Geoscience*, *2*(7), 509-513.

Wilcock, W. S. D., A. D. Stephen, and G. M. Purdy (2002), Microearthquakes on the Endeavour segment of the Juan de Fuca Ridge, *Journal of Geophysical Research*, *107*(B12), doi:10.1029/2001JB000505.

Wilcock, W. S. D., and J. R. Delaney (1996), Mid-ocean ridge sulfide deposits: Evidence for heat extraction from magma chambers or cracking fronts?, *Earth and Planetary Science Letters*, *145*(1-4), 49–64.